Contents lists available at ScienceDirect

Applied Catalysis B: Environmental

Assessment of mechanisms for enhanced performance of Yb/Er/titania photocatalysts for organic degradation: Role of rare earth elements in the titania phase

Vignesh C. Bhethanabotla [a,b], Daniel R. Russell [a], John N. Kuhn [a,*]

[a] *Department of Chemical & Biomedical Engineering, University of South Florida, Tampa FL 33620, United States*
[b] *International Baccalaureate Program at C. Leon King High School Tampa FL 33610, United States*

ABSTRACT

The effect of doping titania with rare earth erbium and ytterbium ions on photocatalytic degradation of a real pollutant (phenol) and a model pollutant was studied under simulated solar radiation and using light of specific frequencies in the ultraviolet, green, red, and infrared regions via LEDs. The goal of this study was to quantify the effect of these dopants on photocatalytic degradation rates and critically assess the phenomena (upconversion, adsorption, recombination kinetics, etc) responsible for improved performance upon rare earth ion doping of titania. A hydrothermal process was modified to synthesize pure anatase and rare earth ion doped TiO_2. The doped catalysts contained 2% Er and 0, 10, 15, or 20% Yb, on an elemental basis. These photocatalysts were characterized for structure, composition, surface area, particle size, bandgap, and band edge positions. The results indicated that the rare earth elements substituted in the titania phases, which were the crystalline anatase and amorphous titania phases. Aqueous-phase photocatalytic degradation rate constants for both organics under a variety of light irradiation conditions were quantified via slurry batch reactor studies in the liquid phase using pseudo first-order kinetics. On reactor volume and catalyst mass bases (same trends due to same catalyst loading), the 2% Er/TiO_2 catalyst performed ∼3× better (compared to ∼10× on surface area basis) and the 2% Er 10%Yb/TiO_2 catalyst performed ∼1.7× (∼3.5× better on surface area basis) than the pure titania sample for phenol degradation under simulated solar irradiation. Though there were minor differences because the model pollutant (Rose Bengal) adsorbed during dark equilibration and phenol did not, similar enhancements were observed for photodegradation of Rose Bengal. Photodegradation was further studied using high-intensity LED irradiation at different narrow wavelengths (405, 530, 660, and 940 nm) which matched the photon absorption energies related to upconversion of the doped samples. Phenol conversion was observed only for the UV (405 nm) source. Similar observations were made for Rose Bengal degradation. A conclusion was reached that upconversion did not contribution to the photocatalytic performance under simulated solar insolation. Combined with the lack of phenol adsorption during dark equilibration for any of the samples, photon energy of the excitation source relative to the band gap and differences in defect chemistry on key kinetic steps are the only plausible explanations for the enhanced performance of these rare earth doped samples compared to pure titania.

1. Introduction

Photocatalysis is a promising field that has the potential of utilizing solar energy in applications such as water splitting, pollutant removal, and conversion of carbon dioxide to useful chemicals [1,2]. Titiania (TiO_2) is the most studied semiconductor catalyst material [3,4]. However, TiO_2 is not feasible for use under solar insolation due to the limitation of its bandgap, which is in the UV range (∼3.0–3.2 eV [5]), as UV light makes up a very small portion (3–5%) of the solar photons that reaches earth. Considerable effort has gone into discovering, tailoring, and modifying semiconductor materials and heterostructures which are stable under reaction conditions and have the potential to absorb visible photons due to their larger availability in the solar spectrum [6,7]. Despite this effort, significant improvements in the reaction rates and photon capture and efficiency (apparent quantum yield) have not been achieved to the

level required for wide implementation. An interesting approach to increase the use of low energy photons in solar insolation is to employ the phenomenon of upconversion, which is the combination of multiple low energy photons to one high energy photon [8], to increase the number of photons of requisite energy for a desired photochemical transformation. Upconversion photocatalysis using rare earth element combined with semiconductors has been the focus of several recent studies in which key findings have contributed to the assessment of its role in improved photocatalytic reaction rates.

Obregon et al. have presented a series of recent articles on the role of upconversion in Er/BiVO$_4$ [9,10], Er/Bi$_2$WO$_6$ [11], and Er/TiO$_2$ [12]. Focusing on the latter study [12], 2% Er/TiO$_2$ was the best performing catalyst for phenol degradation under all five of the light conditions tested (UV, UV–vis, NIR, Vis-NIR, and UV–vis-NIR). From these results and substantial characterization efforts, Obregon et al. concluded that upconversion and decreased charge carrier recombination rates were the two key factors for improved reaction rates. Whereas Obregon et al. [12] reported activity using NIR light and luminescence at ~400 nm from 980 nm excitation as evidence for upconversion in their Er/TiO$_2$ samples, reaction activity was also seen for TiO$_2$ under NIR light despite the lack of luminescence. The discrepancy could be associated to the filters allowing a portion of the unwanted photons for this experiment to pass, which, for example, Obregon et al. reported [12] as 0.2 W/m^2 of UV photons (λ < 400 nm) for the UV and UV–vis conditions.

More recently, Reszczynska et al. published two articles [13,14] on various rare earth metal doped TiO$_2$ catalysts for visible light photodegradation of phenol. In the first article [13], enhanced phenol adsorption and decreased recombination rates were identified as the key factors for improved performance. In the subsequent article [14], only decreased recombination rates were discussed as the reason for improved performance, with different mechanisms for UV and Vis photons. Upconversion was not discussed as a contributor to the improved rates in either study [13,14], despite the catalysts and phenol degradation conditions being similar as in the work by Obregon et al. [12].

Although all studies reviewed here in detail linked enhanced catalytic activity to suppressed recombination rates, the underlying phenomena are likely very different as Obregon et al. [12] claimed the Er was replacing Ti cations in the anatase lattice and Reszczynska et al. [13,14] deduced the various rare earth elements (including Er) were in separate oxide phases. The fact that Obregon et al. found 2%Er/TiO$_2$ as best performing [12] and Reszczynska et al. determined 0.5% Er/TiO$_2$ as best performing (of the Er containing samples) [13,14] suggested that different phenomena could be responsible for the activity enhancements. These structural differences could be induced due to different synthesis procedures as Obregon et al. [12] employed a hydrothermal approach and Reszczynska et al. initially used a sol gel approach [13]. Although at a lower temperature (RT), sol-gel synthesis has much more rapid kinetics (reaction time = 1 h [13]) than hydrothermal synthesis (140 °C, 20 h [12]), due to water acting as a catalyst to enhance the hydrolysis of anionic alkoxide precursors during sol-gel preparation. While most plausible that the structural differences were induced by the kinetic differences, phase segregation could also occur during the post-synthesis calcination. The calcination occurred at 400 °C in air for 2.5 h after the sol-gel synthesis [13], but only at 300 °C in air for 2 h after the hydrothermal synthesis [12]. Phase segregation may be enhanced during calcinations using long times and/or high temperatures. However, in more recent work, Reszczynska et al. [14] used both synthesis techniques and found, for 0.25% Er/TiO$_2$, that the hydrothermal approach yielded smaller segregated rare earth oxide phases and more catalytically active samples, whereas the sol gel approach yielded more luminescence when irradiated with 980 nm photons.

Another important different among these studies was whether phenol adsorbed during dark equilibration. Despite using initial phenol concentrations of 20 ppm and similar samples, Reszczynska et al. reported up to 13.9% phenol removal during 30 min dark equilibration in one study [13] and no phenol adsorption in the other [14]. Obregon et al. used initial phenol concentrations of 30 ppm and did not make any specific mention to phenol adsorption [12]. These different results for phenol adsorption during dark equilibration could be caused by differences in solution properties (e.g., phenol concentration, pH, ionic strength, etc) or by material properties (specific surface area, surface phases and terminations, etc). Adsorption as a primary parameter would be consistent with our previous results, in which composite catalysts comprised of a rare earth doped carrier phase (YAG) adjoined to TiO$_2$ yielded substantial enhancements compared to TiO$_2$ alone even when no rare earth elements were embedded in YAG [15].

In context of the results from recent literature just highlighted, the studies indicate that further examinations are needed to refine the structure-function relationships of rare earth doped titania photocatalysts. The goal of this study is to systematically probe whether upconversion contributes to the visible and NIR induced activity of Er/TiO$_2$ catalysts. Thus, the synthesis and composition (2% Er/TiO$_2$ prepared by the hydrothermal method) of Obregon et al. [12] was followed. This present article is a part of a continuing effort in this topic and follows a recent article [15] in which the rare earth metals are embedded into a host phase rather than the titania phase. To enhance the probability of upconversion and its contribution to photocatalytic activity, Yb was chosen as a sensitizer for Er, as this approach of dual ion upconversion may increase optical absorption in the NIR [13,16–20], where ~40% of the photons in solar insolation reside. In addition to the role of optical properties, the effect of structural modification of TiO$_2$ upon incorporation of these rare earth ions is also considered in this work. These studies are then used to interpret photocatalytic rate enhancements of rare earth doped TiO$_2$ compared to anatase TiO$_2$ under several light conditions including simulated solar light (broadband) and narrow wavelength ranges (using LEDs). Phenol was utilized as the pollutant as it was examined in the referenced studies and is a pollutant of environmental interest [21,22].

2. Experimental section

2.1. Synthesis of the photocatalysts

The photocatalysts were synthesized using a hydrothermal method (following literature procedures [12,23]), which was modified by adding measured amounts of erbium nitrate (Er(NO$_3$)$_3$·5H$_2$O; Sigma-Aldrich, 99.9%) and ytterbium nitrate (Yb(NO$_3$)$_3$·5H$_2$O; Sigma-Aldrich, 99.9%) to the reaction mixture to achieve desired atomic ratios of Ti:Er:Yb. Whereas the ytterbium content varied (0, 10, 15, or 20%), the erbium amount was held constant at 2%. Pure anatase TiO$_2$ was synthesized as a control. The purity of the titanium isopropoxide was >97%.

2.2. Materials characterization

Samples were characterized for their surface area and porosity, crystal structures, bandgaps, band edges, and compositions. X-Ray diffraction measurements were performed on powder samples using the Bruker D8 Advance XRD Instrument. The X-ray source was Cu Kα radiation (0.15406 nm). Diffraction patterns were recorded in the 2θ range of 20°–80° with step size 0.01° and 30 s per step. Crystallite size was determined by Scherrer analysis. Lattice parameter calculations performed with the Profex/BGMN software [24]. Additional patterns were obtained with physical mixtures (1:1 on

mass ratio) of the catalysts samples and ZnO to benchmark the intensities of the samples' diffraction lines against a reference. Raman spectroscopy was conducted with a Horiba T64000 spectrometer using a 532 nm laser as the source.

Specific surface area, pore size distribution, and pore volume were determined by N_2 isotherm measurements at T = 77 K using the Quantachrome Autosorb IQ apparatus following degassing overnight at T = 200 °C. Specific surface area and pore size distribution were determined by the BET and BJH methods, respectively.

Scanning electron microscope (SEM) images were taken using a Zeiss EVO SEM instrument with EDX capability. Average atomic composition analysis was preformed using EDX analysis on several locations.

UV–vis spectra in diffuse reflectance mode were recorded using a JASCO V-670 instrument with the 60 mm integrating sphere attachment. The ground samples were sandwiched between two glass slides in the machine in front of a Spectralon white reflectance standard. The reflectance spectra in the range of 350–1200 nm were used to calculate bandgaps by plotting the Kubelka-Munk function $(1-R)^2/2R$ vs the energy of light (converted from nm to eV), where R is the reflectance [25,26]. The bandgap was calculated by finding the zero of the tangent line at the point of inflection of the Kubelka-Munk function [27,28].

Photoluminensce (PL) emission spectra were collected for all samples using an ISS PC1 Spectrofluorimeter with an excitation wavelength of 290 nm. The samples were held in a quartz solid sample holder at an angle of 45° to the excitation beam.

Electrochemical Impedance Spectroscopy (EIS) was utilized for band edge measurement of the photocatalyst samples. First, a thick slurry of a well-ground sample was spread on pure titanium foil purchased from Sigma-Aldrich. Then, a doctor blade technique was utilized to spread and partially dry the sample. Ti foil of about 2.5 cm by 1.5 cm was utilized. The samples were then oven dried at 250 °C for 5 h, which yielded a smooth film in the middle section of the foil. A sample holder for these semiconductor films was fabricated from a plexiglass slab on which the foil was mounted and connected to the 3 electrodes of an electrochemical cell (working, counter and reference electrodes). A cut-off centrifuge tube was utilized to load the electrolyte (0.1 molar sodium sulfate in water). This electrolyte cell was glued to the sample surface on the Ti foil with epoxy. Two Ti wire electrodes were used as reference and counter electrodes to probe the electrolyte in the cell. The third electrode was connected directly to the Ti foil after removing any oxide that formed on the surface. The Ti wire electrodes were calibrated against a standard $Ag/AgCl_2$ electrode (which fit into the cell), which was later calibrated against a standard calomel electrode (SCE) in the same electrolyte and cell using a multimeter. This was necessitated by the electrochemical cell fashioned for the EIS spectra being too small for the calomel electrode to fit. A potentiostat/galvanostat model Gamry 300 was utilized for the measurements using the EIS software from Gamry. EIS profiles were obtained at 10, 50, 100 and 1000 Hz frequencies. Flatband potentials were calculated by plotting inverse capacitance squared $(1/C^2)$ as a function of voltage, which was found to be independent of frequency for all samples. Conduction band edges were determined using standard equations from these flat band potentials [29,30]. These measurements were made four times on two samples for each of the compositions studied.

2.3. Photocatalysis experiments

A slurry batch reactor was used for the degradation studies. A loading of 1 g/L of the photocatalyst was loaded into the dye solution, which was constantly stirred using a magnetic stir bar. A plastic holder was machined to house two high-intensity LEDs (Thor Labs) of specific narrow-
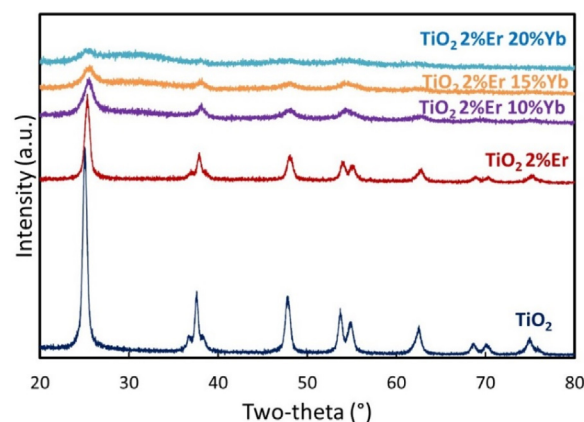

Fig. 1. XRD profiles of the photocatalysts. Increasing Yb concentration led to a decrease in crystallinity. Profiles are offset for clarity.

distribution wavelengths in the UV (405 nm; Pmax = 760 mW; FWHM = 13 nm), green (530 nm; Pmax = 370 mW; FWHM = 33 nm), red (660 nm; Pmax = 700 mW; FWHM = 25 nm) and NIR (940 nm; Pmax = 1000 mW; FWHM = 37 nm) ranges. Fresh catalyst samples were used for all photocatalytic experiments. Using procedures described previously [31], additional studies were conducted under broadband illumination that simulated the solar spectrum. In the narrow spectrum experiments, LEDs were utilized at full intensity. Light intensities at the liquid interface were measured for the broadband and UV LED illuminations using a Fieldmax-TOP Energy meter and a ThorLabs PM100D Compact Power and Energy Meter with a ThorLabsS121C Standard Photodiode Power Sensor, respectively. In initial experiments, Rose Bengal dye was used as a model for pollutants, as its structure is similar to many common pollutants. In addition, degradation experiments were conducted using phenol, a common pollutant of environmental interest. The initial concentrations of the reactants were 20 ppm for Rose Bengal and 10 ppm for phenol. Whereas there was no adsorption of phenol during the dark equilibration time, adsorption of Rose Bengal occurred and was accounted to ensure the initial concentration for the reaction studies was 20 ppm. Organic concentrations (540 nm for Rose Bengal and the 270 nm for phenol) were analyzed using UV–vis spectroscopy (PerkinElmer model Lambda 35) as a function of reaction time by removing small aliquots. The pH (Oakton pH+ meter with Hanna HI1131 probe) and the total organic carbon (Hach TOC kit) were employed in select experiments to monitor changes between initial and final values. The reaction results were interpreted using a batch reactor model with first order kinetics. In a previous study [15], errors in the rate constant were less than 10% of the reported values.

3. Results and discussion

3.1. Structural and compositional characterization

The XRD profiles (Fig. 1) indicated that all samples are of the anatase phase (JCPDS card 78-2486, corresponding to the I41/*amd* space group). The major indicative diffraction lines corresponding to the anatase phase are (101) at 25.4°, (103), (004), and (112) near 38°, (200) at 48.1°, (105) and (211) near 55°, and the (204) at 62.9°. The XRD results did not indicate the presence of any other phases of TiO_2. The incorporation of Er (89.0 pm; trivalent VI coordination) and Yb (86.8 pm; trivalent VI coordination) did not alter the crystalline phase even though these ionic radii are larger than that of Ti (60.5 pm; tetravalent VI coordination). However, the addition of rare earth metals did lead to decrease in crystallinity. These findings were determined more conclusively by conducting XRD of

Table 1
Physiochemical properties as a function of Er and Yb doping into TiO$_2$.

Photocatalyst	Specific Surface Area (m^2/g) [a]	Pore Diameter (nm) [a]	Pore Volume (cm^3/g) [a]	Crystallite Size (nm) [b]	I$_{TiO2}$/I$_{ref}$ [c]	Molar Ratios Ti:Er:Yb [d]
Pure TiO$_2$	312.5	14.9	0.77	16	0.14	100:00:00
TiO$_2$/2%Er 0%Yb	98.1	14.9	0.32	14	0.22	98:02:00
TiO$_2$/2%Er 10%Yb	151.4	14.9	0.50	7.5	0.13	87:02:11
TiO$_2$/2%Er 15%Yb	109.4	14.9	0.28	7.8	0.039	84:02:14
TiO$_2$/2%Er 20%Yb	171.1	9.8	0.42	6.2	0.030	76:02:22

[a] Determined by N$_2$ physisorption.
[b] Determined by Scherrer analysis of XRD profiles.
[c] Determined by XRD analysis of catalysts physically mixed with ZnO reference (ref.). Intensity (I) ratio of most intense anatase TiO$_2$ line divided by most intense ZnO line.
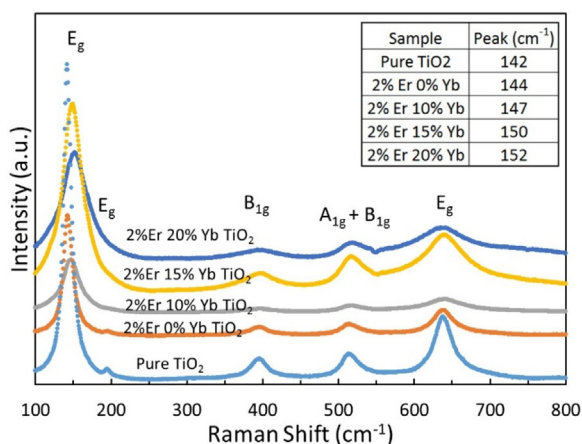[d] Determined by EDS.

Fig. 2. Raman spectra of the photocatalysts. Increasing Yb concentration led to shift of one Eg vibration (∼150 cm^{-1}; see insert) and disappearance of another (∼200 cm^{-1}). Profiles are offset for clarity.

Table 2
Lattice parameter analysis from XRD results.

Photocatalyst	a (Å)	c (Å)	c/a	V(Å^3)
Pure TiO$_2$	3.7859	9.5071	2.511	136.26
TiO$_2$/2%Er 0%Yb	3.7883	9.5033	2.509	136.38
TiO$_2$/2%Er 10%Yb	3.8101	9.5065	2.495	138.01
TiO$_2$/2%Er 15%Yb	3.8228	9.5334	2.494	139.32
TiO$_2$/2%Er 20%Yb	3.8352	9.5576	2.492	140.58

the samples physically mixed with a reference material (i.e., ZnO) without overlapping diffraction lines. The results are shown in Fig. S1. The quantification of the intensity ratio of the main anatase TiO$_2$ diffraction line to the main ZnO diffraction line (Table 1) indicated that the high levels of Yb doping spurred the transition to the amorphous phases. The sample with the highest concentration of Yb^{3+} (20%) comprised primarily of an amorphous phase. As a result, other phases could exist as amorphous in the samples. Despite the size differences between Ti and the rare earth metals, an oxygen deficiency induced into the titania host would substantially facilitate substitutional doping, as the ionic radius of 6-coordinated Ti increases from 60.5 to 67 and 86 pm as the valence of Ti decreases from tetravalent to trivalent to divalent, respectively.

Sherrer analysis (Table 1) indicated that crystallite size progressively decreased from 16 to 6.2 nm upon increasing concentrations of the rare earth ions. This trend could be attributed to the lanthanide oxides preventing anatase particles from adhering together, thus inhibiting growth of crystal grains. A similar explanation was been proposed for addition of rare earth metals to titania by incipient wetness impregnation [32].

The structural features of the photocatalyst samples was also examined by Raman spectroscopy, which is able to discriminate the various phases of titania [12,33,34]. As shown in Fig. 2, the spectra all matched that of pure titania. Each spectrum contained the 6 peaks associated with the anatase phase, and no other vibrations were measured. Moreover, peak positions are aligned with measurements by Haro-Poniatowski et al. [33] which suggested that the samples are comprised of only anatase or mixture of anatase and amorphous phases, with none being only amorphous. In light of the XRD results which showed increasing amorphous nature at high dopant levels, these samples are a mixture of anatase and amorphous phases for all doped samples in this study. Additionally, the intensities of the bands generally decreased with doping. As

the E$_g$, A$_{1g}$, and B$_{1g}$ bands are respectively associated to symmetric stretching, symmetric bending, and asymmetric bending vibrations of O—Ti—O [34,35], the intensity losses indicated disruption of the Ti centers within the anatase lattice, which would be consistent with rare earth metal replacement on the Ti sites. Finally, the main peak (E$_g$ ∼ 150 cm^{-1}) shifted to lower wavenumber with increasing rare earth doping (Fig. 2 insert). This trend was consistent with the results of Obregon et al. [12], who concluded that rare earth ions were contained within the anatase lattice (Table 2).

The N$_2$ porosimetry results (Table 1) indicated relatively large surface areas for the samples in the range of 100–300 m^2/g, which is consistent [12] with previous rare earth doped TiO$_2$ studies. All samples showed type IV isotherms. The specific surface areas and pore volumes generally decreased with increasing dopant amount. This trend could be caused by amorphous phases plugging portions of the pore volume. The pore diameters and distributions were similar for all samples except the sample with 2% Er and 20% Yb. This sample likely behaved differently due to its mostly amorphous nature, which could also be reflected in its different porosity than the other samples. The pure TiO$_2$ sample showed substantially larger specific surface area compared to the rare earth ion doped samples, which could be associated to a high number of pores as the pore volume was also much higher for this sample. This sample demonstrated a different hysteresis loop than the other samples. Whereas all the doped samples showed hysteresis behavior indicative of cylindrical pores, the hysteresis loop for the pure titania sample was consistent with slit or conical pores. This difference was likely the source of the larger surface area and pore volume for the pure titania sample in comparison to the doped samples and may reconcile the differences in surface area despite similar crystallite size when compared to the 2% Er/TiO$_2$ sample.

SEM images, shown in Fig. 3, indicated loosely agglomerated particles when viewed at 1 μm scale. Visually, a trend of increasing amorphous nature with increasing dopant amounts emerged. EDS data were utilized to calculate the molar ratios of Ti:Er:Yb, with results compiled in Table 1. The spectra clearly indicated peaks above ∼5 keV (where only Er and Yb would contribute) for all samples except the pure TiO$_2$. The tabulated values closely matched the concentration ratios used in the initial precursors amounts. In addition, as presented in Fig. 3(f), the oxygen content increased with the initial doping amount of both 2% Er and 2% Er/10% Yb, before decreasing slightly to lower values for the 2% Er/15% Yb and 2% Er/20% Yb. Since the nominal oxidation state of Er and Yb is lower than TiO$_2$, this finding suggested that Er and Yb are not forming
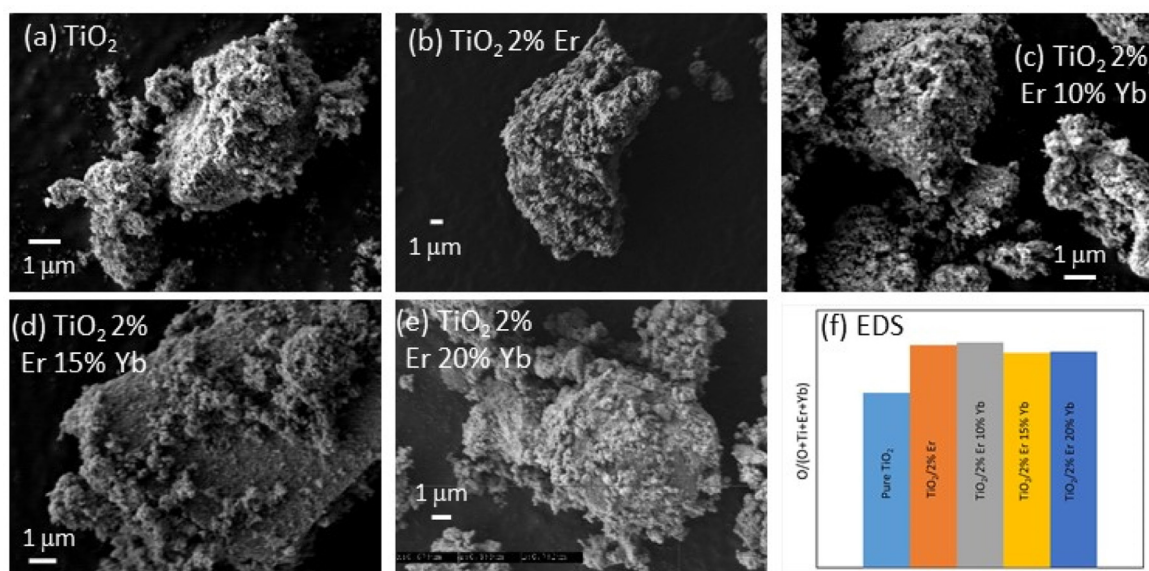
Fig. 3. SEM images and example EDS data for (a) Pure TiO_2, (b) TiO_2 2% Er, (c) TiO_2 2% Er 10% Yb, (d) TiO_2 2% Er 15% Yb, (e) TiO_2 2%Er 20% Yb, and (f) Comparison of atomic oxygen amounts (O/(O + Ti + Er + Yb))from EDS averages.

separate oxides phases for at least the 2% Er/15% Yb and 2% Er/20% Yb samples. The atomic oxygen fraction was approximately 0.67 for all samples with slightly higher values for the 2% Er and 2% Er/10% Yb.

To summarize this section, the structural characterization results suggested that rare earth substitution on Ti sites in both anatase and amorphous titania phases, which co-exist upon doping by these rare earth elements. From inference of the Raman spectra, either the anatase phase only or a mixture of the anatase and amorphous titania phases existed. Due to the increasing amorphous nature of the samples with doping, as observed by XRD, the latter case (anatase and amorphous titania mixture) is the most probable situation. EDS results are also in agreement with rare earth ion doping into the titania phases for these samples, with the results especially supporting this hypothesis for the two samples with lower rare earth ion doping. In addition, as will be discussed in the next section, Yb doping has a substantial quenching effect on Er's optical properties in TiO_2 and this effect would also be in agreement with both ions being in the same lattice structure. Due to the slightly different nature of the highest-doped sample (TiO_2 with 2% Er and 20% Yb) observed in some of the characterization studies and its highly amorphous nature, this sample may be an exception to the overall picture developed in this study. However, as a summary, rare earth replacement of the Ti sites in the two titania phases is fairly conclusive from the characterization data and their analyses.

3.2. Optical and electronic characterization

The PL spectra from the 5 samples excited with UV light (290 nm) are shown in Fig. 4. Each sample has peaks at the approximate values of 360, 390, 400, 425, and 470 nm. Since each features are present even in the pure TiO_2 sample and that it has an indirect bandgap, the results suggested that Er and Yb doping have a distinct effect on the defect chemistry of the host TiO_2 anatase structure, rather than indicating features of new phases formed. Although non-linear, relative intensity below emission wavelengths of 410 nm increased with increasing dopant amount. The broad intensity below 410 nm are presumed to be caused by distortions in the anatase lattice induced by defects. The peak at 390 could be attributed to electron transitions from conduction band minimum to valence band maximum [36]. Raman scattering by
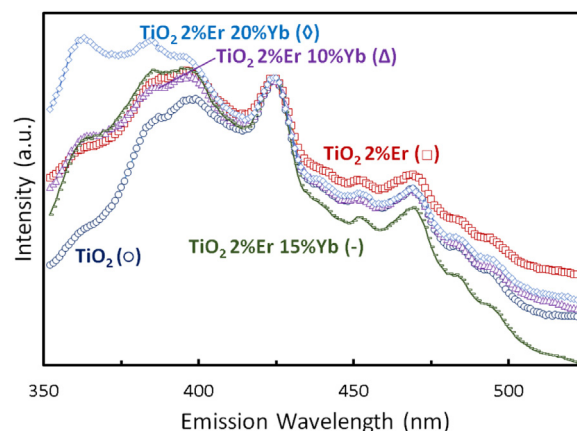

Fig. 4. PL spectra of the samples. The excitation source is 290 nm. Spectra are normalized to peak at 425 nm.

adsorbed water and oxygen vacancies with 2 trapped electrons may also influence the relative intensities of the 360 nm peak [37] and 400 nm peak [36], respectively. According to literature [12,14,38], the peaks in the ~410–450 nm range are associated to bulk charge carrier recombination caused by shallow defects near the valence band. The peak at ~470 nm is associated to oxygen vacancies in the anatase lattice [12,36,39]. The relative intensity of this feature is most prevalent in one (2% Er/TiO_2) of the more active samples, which suggests that this structural feature is important for photocatalytic activity.

Diffuse reflectance UV–vis spectra (Fig. 5) indicated that doping with Er^{3+} and Yb^{3+} produces absorption peaks in the visible and NIR ranges whose intensities depend upon the rare earth ion concentrations. These peaks are associated with the possibility of upconversion. No such peaks were observed for the pure TiO_2 sample. The samples containing Er^{3+} demonstrated the large peaks in the UV, green and red regions of the visible spectrum correlating to known electronic transitions. For Er^{3+}, transitions from the ground state $^4I_{15/2}$ to the higher energy levels $^4F_{7/2}$, $^4S_{3/2}$, $^4F_{9/2}$ and $^4G_{9/2}$ show absorption at 489, 520, 653 and 800 nm, respectively [12], which are all visible in the reflectance spectrum of these DRS measurements. The intensities of these peaks decreased as Yb con-
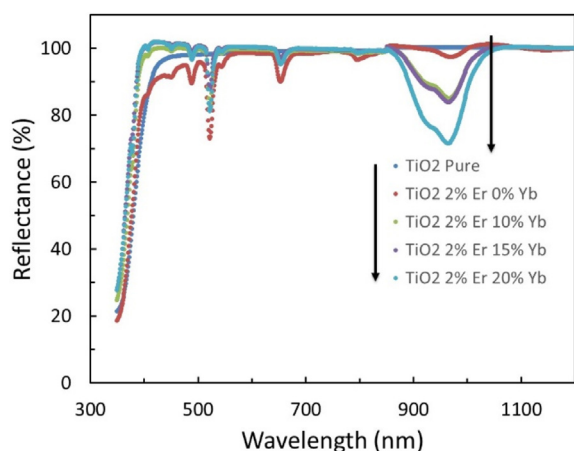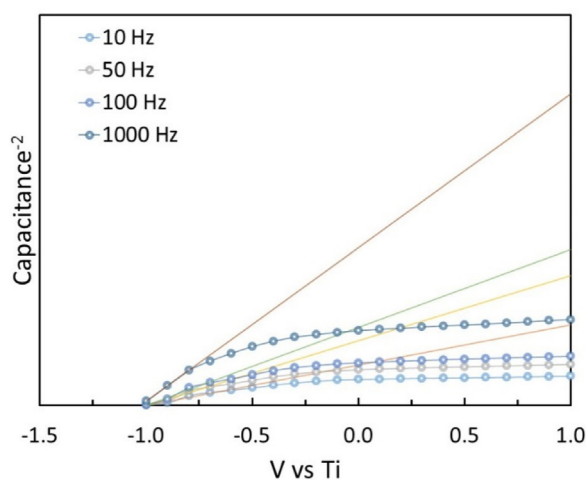
Fig. 5. DRS for the samples.

Fig. 6. Mott Schottky Plot for determining the flatband potential for the 0% Yb photocatalyst.

Fig. 7. First-order rate constants for the phenol degradation reaction in batch slurry reactor. [a]Solar stands for simulated solar (I = 200 W/m^2). UV stands for UV LED (I = 500 W/m^2). Vol. means rate constant on reactor volume basis. Area means rate constant on catalyst surface area basis. Negligible conversions measured (<1% over 2 h) for LEDs of wavelength 530, 660, and 940 nm [b]Rate constant per reactor volume (k). [c]Rate constant per catalyst surface area (k").

centration increased in these systems. This trend was likely caused by saturation of Er's absorption properties as neighboring excited Yb caused quenching [8]. In addition, in the NIR, the TiO$_2$ with 2%Er has a small peak at 980 nm, which corresponded to the $4I_{11/2}$ transition. The intensity of this peak increased with increasing Yb^{3+} concentration. This finding was expected as Yb and Er are a very common rare earth metal combination for increased IR absorption [13,16–20].

From the UV portion of the DRS results (Fig. 5), Tauc plots were constructed and analyzed to determine the band gap. As suggested from the DRS data, a minimal change to the band gap of TiO$_2$ occurred. The specific values ranged from 3.10 to 3.18 eV and are compiled in Table 3. These values are all within the general range of anatase TiO$_2$, which is reported [40,41] to be ~3.2 eV. Red shifts of the band gap have been reported to occur for rare earth doping for both cases when the metals are within the lattice [12] and when metals are in separate phases [13,32]. This effect can be eliminated by doping the rare earth metals into a host phase separate from the semiconductor phase (minimizing rare earth-Ti interactions) as in our recent work [15].

An electrochemical approach was utilized to measure the conduction band edge positions. A representative Mott Schottky plot used to determine the flatband potential is shown in Fig. 6. This flatband potential was then used to calculate the position of the conduction band (Table 3). The example Mott Schottky plot in Fig. 6 indicated that similar voltages were determined regardless
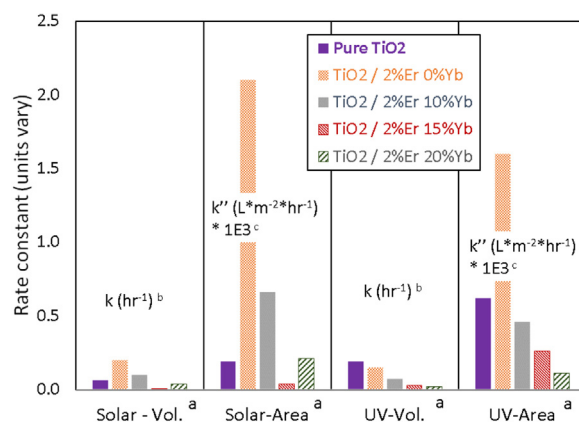
of the frequency used, as it should be for the analysis. The valence band positions were then calculated by combining with the DRS-determined bandgaps. The obtained values of the conduction band edge closely match that of anatase TiO$_2$ in the literature. The conduction band edge of TiO$_2$ is reported to be slightly negative on the NHE scale (~ −0.5 eV [41,42]). The values in Table 3 range from −0.8 to −1 eV vs SCE, which converts to −0.56 to −0.76 eV on the NHE scale. Thus, the differences in the band edge positions and band gaps upon doping with Er and Yb are minor. This conclusion is consistent with doping of Er into oxide semiconductors [9,10,12], but it is noted that a maximum of 4% Er was used in those studies, whereas the current study used up to 22% rare earth metals.

3.3. Photocatalytic activity

The first order rate constants determined for phenol and Rose Bengal under simulated solar insolation conditions and under UV LED irradiation (for phenol) are shown in Fig. 7 (and Table S1) and Table S2, respectively. The batch slurry reactions were conducted on an equal volume and equal mass basis, so the rate constants on a catalyst mass basis (not calculated) would follow the same trend as the rate constants on a volume basis. No phenol adsorption was observed during the dark equilibration. Adsorption of Rose Bengal was accounted during preparation of initial concentrations for the reactor studies. Since the specific surface areas varied for the samples, the rate constants on a surface area basis were also calculated. The surface area normalized rate constants are important for practical reasons as immobilized film catalysts are commonly used to avoid powder recovery issues [15,43].

In addition, the phenol photodegradation experiments were conducted under five different light conditions as denoted in Table S1. Phenol conversion only occurred under the broadband and UV LED irradiation. This lack of phenol conversion under the NIR LED (centered at 940 nm) was surprising considering the substantial conversion reported by Obregon et al. using wavelengths greater than 800 nm [11] and DRS profiles (Fig. 5) showed substantial optical activity for the samples containing Yb and Er in the range of 880–1020 nm. The two visible light LEDs (centered at 530 and 660 nm) were also substantially aligned with the optical activity of Er (Fig. 5). Accordingly, upconversion was not deemed to contribute to the photocatalytic activity of these samples under any of the light sources.

Substantial activity and differences among the samples were noted under UV LED and simulated solar irradiation. On reactor

Table 3
Band gaps and band edges of the photocatalysts.

Photocatalyst	Bandgap (eV)[a]	Conduction Band Edge vs SCE (eV)[b]	Valence Band Edge vs SCE (eV)[c]
Pure TiO$_2$	3.10	-0.9 ± 0.01	2.2 ± 0.01
TiO$_2$/2%Er 0%Yb	3.13	-0.8 ± 0.007	2.3 ± 0.007
TiO$_2$/2%Er 10%Yb	3.17	-1 ± 0.022	2.2 ± 0.022
TiO$_2$/2%Er 15%Yb	3.18	n.m.	n.m.
TiO$_2$/2%Er 20%Yb	3.17	n.m.	n.m.

n.m. denotes not measured.
[a] Determined by Tauc plot.
[b] Determined by EIS.
[c] Calculated from conduction band edge and bandgap.

volume and catalyst mass bases, two distinct trends with increasing rare earth doping were observed under the two light conditions. With the UV LEDs, the rate constant (k) decreased monotonically with increasing doping level whereas a maximum rate constant was achieved near samples with 2% Er and 2% Er/10%Yb in the presence of simulated solar insolation. The trend under UV LEDs can be explained by suitable light availability for the samples based on the band gap. The UV LED emits light centered at a wavelength of 405 nm (3.06 eV), which is a lower energy than all of the band gaps (Table 3). Based on the band gaps, the maximum wavelength (minimum energy) of light needed for absorption by the sample decreased from ~400 nm to ~390 nm with increasing dopant amount. Based on the emission spectrum of the UV LED (peak at 405 nm with measureable intensity ranging from 385 to 435 nm), approximately 25% and 1% of the emitted energy would be available for band gaps of 3.10 and 3.18 eV, respectively. This analysis is also consistent with the PL spectra (Fig. 4), as the relative PL intensity at low wavelengths increased with increasing dopant amount. Since the band gaps of the 3 highest doped samples were similar, trends with composition are possible and will be discussed in analyses of the broad band light.

The phenol photodegradation experiments with broad band light indicated maximum rate constants for the titania samples doped with 2% Er and 2%Er/10% Yb. Further doping contributed to decreased rate constants. The light cutoff at the low wavelength end for this light source was 375 nm (3.31 eV), meaning that the differences in band gap of the samples did not contribute to the trends. Using the pure titania sample as an illustration because its band gap best matched the UV LED, the rate constant was ~3 times higher under the UV LED than the simulated solar irradiation. Even though only a fraction of the UV LED emissions (~25% or 125 W/m^2) was available for absorption, this value is higher than the UV portion of the broadband light (~10% or 20 W/m^2). These results would agree with positive order dependence of the rate constant on the useable photon intensity, as has been reported by Nimlos et al. [44]. Further studies beyond the scope of this paper would be required to determine the order of this effect. Finally, even though it is difficult to compare rates from literature studies due to a myriad of variable conditions, a survey of the recent literature on rare earth doping effects for phenol degradation rates under broadband light is compiled in Table 4. A key feature is that rare earth doping improved performance compared to pure titania and P25 by up to a factor of 4. In addition, the importance of following conventional standards (such as 1 g/L catalyst loading which has been identified as or near optimal previously and consistently [21,45]) and conducting thorough light characterization as done in the current study are key features to make future comparisons more precise.

In addition to the catalytic activity, pH and total organic carbon (TOC) were monitored in select phenol photodegradation experiments under simulated solar insolation. Minimal pH changes were measured. For the 5 experiments, the initial pH values were 5.7 and, over 2 h in the presence of the simulated solar irradiation, the pH was within 0.2 of the initial value. This pH value is slightly lower

than the point of zero charge (PZC) for TiO$_2$ (~5.8–6.25 [43]) indicating a fairly neutral surface and consistent with the lack of phenol adsorption during dark equilibration. For the 2% Er/TiO$_2$ catalyst, the TOC analysis indicated 22.5% conversion of total carbon over 2 h of reaction time. Over the same time window, the phenol conversion was judged to be slightly higher (29%). The most likely products which contribute to this difference are benzoquinone, hydroquinone, and short chained organic acids, which have been observed as intermediates quantities from aqueous phenol photodegradation [13,21]. So, even though the TOC conversion lagged slightly behind the phenol conversion, the results suggested that total oxidation should be attainable with slightly longer reaction times.

In addition to the reactor volume and catalyst mass bases just described, a comparison of rate constants on a catalyst surface area basis (surface site basis) is also of interest due to potential future experiments on catalyst films. On this basis, the 2% Er/TiO$_2$ catalyst performed ~10× better (compared to ~3× on mass basis) and the 2% Er 10% Yb/TiO$_2$ catalyst performed ~3.5× better (compared to ~1.7× on mass basis) than the pure titania sample. The phenol degradation results presented a clear case, with the doped samples at low Yb loadings showing the best performance on both per mass and the per surface area basis. Since phenol adsorption and upconversion have been rigorously determined to not contribute to the enhanced performance, photon energy of the incident light relative to the band gap and defect structure (from PL spectra intensity below ~400 nm) and suppressed charge carrier recombination rates (induced by defects in the anatase phase) were deemed as the primary phenomena contributing to the performance enhancements.

From literature, X-ray photoelectron spectroscopy (XPS) results for Er incorporation (without Yb) in hydrothermal synthesis technique [12] indicated a decrease in the O/Ti ratio and an increase in the Er/Ti ratio, as the concentration of the Er increased. These results are consistent with the EDS results and PL spectra of the current study and would indicate a valance electron deficiency at the impurity sites caused by oxygen deficiency induced by trivalent doping on tetravalent sites. These sites could then form electron scavenging sites, leading to potential influence on electron/hole recombination rates, and the possibility of increased oxidation rates from the free holes in the structure. Conclusive evidence would require experimental techniques beyond the scope of this work.

To further probe the performance of the samples, photodegradation of the Rose Bengal dye was also studied under several light sources (Table S2). Again, no conversion was measured when using the 660 and 940 nm LEDs. Conversion was observed under the 530 nm light without the catalysts due to the dye induced photolysis. So, these results cannot be included in the analysis. For this dye, substantial adsorption was measured during dark equilibration. This finding was in superb agreement with our previous work [15] in which YAG/TiO$_2$ composites were tested. Due to this adsorption, the pure titania sample was the best performing cat-

Table 4
Comparison of phenol degradation rates under broadband light from recent studies on rare earth doped titania.

Catalyst	Initial Rate (μmol/L/h)	Initial Phenol concentration (ppm)	Catalyst loading (g/L)	Temperature (°C)	Light Intensity (W/m^2)	Reference
2% Er/TiO$_2$	144	30	1	Not reported	627[a]	[12]
TiO$_2$	83					
0.5% Er/TiO$_2$	53.1	20	10	15	Not reported	[13]
TiO$_2$	31.9					
P25	12.9					
2% Er/TiO$_2$	21	10	1	20	200	This study
TiO$_2$	6.3					

[a] lamp irradiance reported.

alyst on a mass basis (Table S2). On a catalytic site basis (surface area basis), several doped samples outperformed the pure titania sample. The 2% Er/TiO$_2$ sample showed the largest rate constant on this basis, ~2.5× times larger than that of pure anatase. For this dye, adsorption and suppressed charge carrier recombination rates were linked to the improved performances.

4. Conclusions

A comprehensive examination of rare earth doping into a titania has been completed. A thorough characterization analysis by a variety of techniques indicated incorporation of Er and Yb ions into the titania phase which include amorphous and anatase components. The argument for incorporation is especially strong at low dopant levels. The rare earth dopants enhanced the aqueous-phase photodegradation of phenol (and Rose Bengal to a lesser degree) at low loadings under simulated solar irradiation, with enhancements varying by catalyst composition. By employing LEDs of specific frequencies to match potential upconversion effects, no contribution to the performance via upconversion was observed. Since phenol showed insignificant adsorption, available photon energy of the excitation source relative to the band gap and differences in the defect chemistry (quantity and nature of defects) on kinetic rates were the only explanations possible for the observed results.

Appendix A. Supplementary data

Supplementary data associated with this article can be found, in the online version, at http://dx.doi.org/10.1016/j.apcatb.2016.09.008.

References

[1] B. Kumar, M. Llorente, J. Froehlich, T. Dang, A. Sathrum, C.P. Kubiak, Photochemical and photoelectrochemical reduction of CO$_2$, Annu. Rev. Phys. Chem. 63 (2012) 541–569.

[2] A. Kudo, Y. Miseki, Heterogeneous photocatalyst materials for water splitting, Chem. Soc. Rev. 38 (2008) 253–278.

[3] J. Schneider, M. Matsuoka, M. Takeuchi, J. Zhang, Y. Horiuchi, M. Anpo, D.W. Bahnemann, Understanding TiO$_2$ photocatalysis: mechanisms and materials, Chem. Rev. 114 (2014) 9919–9986.

[4] M.R. Hoffmann, S.T. Martin, W.-I. Choi, D.W. Bahnemann, Environmental applications of semiconductor photocatalysis, Chem. Rev. 95 (1995) 69–96.

[5] V.P. Indrakanti, J.D. Kubicki, H.H. Schobert, Photoinduced activation of CO$_2$ on Ti-based heterogeneous catalysts: current state, chemical physics-based insights and outlook, Energy Environ. Sci. 2 (2009) 745–758.

[6] S.J.A. Moniz, S.A. Shevlin, D.J. Martin, Z.-X. Guo, J. Tang, Visible-light driven heterojunction photocatalysts for water splitting – a critical review, Energy Environ. Sci. 8 (2015) 731–759.

[7] T. Takata, C. Pan, K. Domen, Recent progress in oxynitride photocatalysts for visible light driven water splitting, Sc. Technol. Adv. Mater. 16 (2015) 1–18.

[8] F. Auzel, Upconversion and anti-stokes processes with f and d ions in solids, Chem. Rev. 104 (2004) 139.

[9] S. Obregón, G. Colon, Heterostructured Er3 + doped BiVO4 with exceptional photocatalyticperformance by cooperative electronic and luminescencesensitization mechanism, Appl. Catal. B: Environ. 158–159 (2014) 242.

[10] S. Obregón, S.W. Lee, G. Colon, Exalted photocatalytic activity of tetragonal BiVO4 by Er3+ doping through a luminescence cooperative mechanism, Dalton Trans. 43 (2014) 311–316.

[11] S. Obregón, G. Colón, Erbium doped TiO2–Bi2WO6 heterostructure with improved photocatalytic activity under sun-like irradiation, Appl. Catal. B: Environ. 140–141 (2013) 299–305.

[12] S. Obregón, A. Kubacka, M. Fernández-García, G. Colón, High-performance Er3 + −TiO2 system: dual up-conversion and electronic role of the lanthanide, J. Catal. 299 (2013) 298–306.

[13] J. Reszczynskaí, T. Grzyb, J.W. Sobczak, W. Lisowski, M. Gazda, B. Ohtani, A. Zaleska, Visible light activity of rare earth metal doped (Er3+, Yb3+ or Er3+/Yb3+) titania photocatalysts, Appl. Catal. B: Environ. 163 (2015) 40–49.

[14] J. Reszczynskaí, T. Grzyb, Z. Wei, M. Klein, E. Kowalska, B. Ohtani, A. Zaleska-Medynska, Photocatalytic activity and luminescence properties of RE^{3+} TiO$_2$ nanocrystals prepared by sol–gel and hydrothermal methods, Appl. Catal. B: Environ. 181 (2016) 825.

[15] J.W. Pickering, V.R. Bhethanabotla, J.N. Kuhn, Assessment of mechanisms for enhanced performance of TiO2/YAG: Yb + 3, Er + 3 composite photocatalysts for organic degradation, (2016) doi: 10.1016/j.apcatb.2016.09.007.

[16] J. Silver, M.-I. Martinez-Rubio, T.G. Ireland, G.R. Fern, R. Withnall, The effect of particle morphology and crystallite size on the upconversion luminescence properties of erbium and ytterbium Co-doped yttrium oxide phosphors, J. Phys. Chem. B 105 (2001) 948–953.

[17] F. Gonnell, M. Haro, R.S. Sanchez, P. Negro, I. Mora-Sero, J. Bisquert, B. Juliaín-Loípez, S. Gimenez, Photon up-conversion with lanthanide-doped oxide particles for solar H2 generation, J. Phys. Chem. C 118 (2014) 11279–11284.

[18] G. De, W. Qin, J. Zhang, J. Zhang, Y. Wang, C. Cao, Y. Cui, Upconversion luminescence properties of Y2O3:Yb3+ Er3+ nanostructures, J. Lumin. 119–120 (2006) 258–263.

[19] F. Huang, X. Liu, Y. Ma, S.C. Kang, L. Hu, D. Chen, Origin of near to middle infrared luminescence and energy transfer process of Er31/Yb31co-doped fluorotellurite glasses under different excitations, Sci. Rep 5 (2015) 8233.

[20] X. Wu, S. Yin, Q. Dong, B. Liu, Y. Wang, T. Sekino, S.W. Lee, T. Sato, UV, visible and near-infrared lights induced NOx destruction activity of (Yb,Er)-NaYF4/C-TiO2 composite, Sci. Rep 3 (2918) (2013) 1–8.

[21] S. Ahmed, M.G. Rasul, W.N. Martens, R. Brown, M.A. Hashi, Heterogeneous photocatalytic degradation of phenols in wastewater: a review on current status and developments, Desalination 261 (2010) 3–18.

[22] J.-M. Herrmann, Heterogeneous photocatalysis: fundamentals and applications to the removal of various types of aqueous pollutants, Catal. Today 53 (1999) 115–129.

[23] S. Jeon, P.V. Braun, Hydrothermal synthesis of Er-doped luminescent TiO2 nanoparticles, Chem. Mater. 15 (2003) 1256–1263.

[24] N. Döbelin, R. Kleeberg, Profex: a graphical user interface for the Rietveld refinement program BGMN, J. Appl. Crystallogr. 48 (2015) 1573–1580.

[25] P. Kubelka, F. Munk, A contribution to the optics of pigments, Z. Tech. Phys. 12 (1931) 593–599.

[26] E.L. Simmons, Diffuse reflectance spectroscopy: a comparison of theories, Appl. Opt. 14 (1975) 1380–1386.

[27] O. Stenzel, The Physics of Thin Film Optical Spectra: An Introduction, Springer Science & Business Media, 2016, pp. 2005.

[28] J. Tauc, Optical properties and electronic structure of amorphous Ge and Si, Mat. Res. Bull. 3 (1968) 37–46.

[29] A.M. Martinez, L.G. Arriaga, A.M. Fernandez, U. Cano, Band edges determination of CuInS2 thin films prepared by electrodeposition, Mater. Chem. Phys. 88 (2004) 417–420.

[30] F. Cardon, W. Gomes, On the determination of the flat-band potential of a semiconductor in contact with a metal or an electrolyte from the Mott-Schottky plot, J. Phys. D: Appl. Phys. 11 (1978) L63.

[31] S.L. Pettit, C.H. McCane, J.T. Wolan, J.N. Kuhn, Synthesis and characterization of composite photocatalytic semiconductors (InVO4-TiO2) using pure and mixed phase titania powders, Catal. Lett. 43 (2013) 772–776.

[32] K.M. Parida, N. Sahu, Visible light induced photocatalytic activity of rare earth titania nanocomposites, J. Mol. Catal. A: Chem. 287 (2008) 151–158.

[33] E. Haro-Poniatowski, R. Rodriguez-Talavera, M. de la Cruz Heredia, O. Cano-Corona, R. Arroyo-Murillo, Crystallization of nanosized titania particles prepared by the sol-gel process, J. Mater. Res. 9 (1994) 2102–2108.

[34] T. Ohsaka, F. Izumi, Y. Fujiki, Raman spectrum of anatase, TiO_2, J. Raman Spec. 7 (1978) 321–324.

[35] F. Tian, Y. Zhang, J. Zhang, C. Pan, Raman spectroscopy a new approach to measure the percentage of anatase TiO_2 exposed (001) facets, J. Phys. Chem. C 116 (2012) 7515–7519.

[36] B. Choudhury, M. Dey, A. Choudhury, Shallow and deep trap emission and luminescence quenching of TiO_2 nanoparticles on Cu doping, Appl. Nanosci. 4 (2014) 499–506.

[37] F.J. Knorr, J.L. McHale, Spectroelectrochemical photoluminescence of trap states of nanocrystalline TiO_2 in aqueous media, J. Phys. Chem. C 117 (2013) 13654–13662.

[38] F.J. Knorr, D. Zhang, J.L. McHale, Influence of TiCl4 treatment on surface defect photoluminescence in pure and mixed-Phase nanocrystalline TiO_2, Langmuir 23 (2007) 8686–8690.

[39] D. Li, H. Haneda, S. Hishita, N. Ohashi, Visible-light-driven N-F-codoped TiO2 photocatalysts. 2. Optical characterization, photocatalysis, and potential application to air purification, Chem. Mater. 7 (2005) 2596–2602.

[40] Y. Mi, Y. Weng, Band alignment and controllable electron migration between rutile and anatase TiO_2, Sci. Rep. 5 (2015) 11481–11482, 11410.

[41] S.N. Habisreutinger, L. Schmidt-Mende, J.K. Stolarczyk, Photocatalytic reduction of CO_2 on TiO_2 and other semiconductors, Angew. Chem. Int. Ed. 52 (2013) 7372–7408.

[42] S.C. Roy, O.K. Varghese, P. Paulose, C.A. Grimes, Toward solar fuels: photocatalytic conversion of carbon dioxide to hydrocarbons, ACS Nano 4 (2010) 1259–1278.

[43] S.L. Pettit, L. Rodriguez-Gonzalez, J.T. Michaels, N.A. Alcantar, S.J. Ergas, J.N. Kuhn, Parameters influencing the photocatalytic degradation of geosmin and 2-methylisoborneol utilizing immobilized TiO2, Catal. Lett. 144 (2014) 1460–1465.

[44] M.R. Nimlos, W.A. Jacoby, D.M. Blake, T.A. Milne, Direct mass spectrometric studies of the destruction of hazardous wastes. 2. Gas-phase photocatalytic oxidation of trichloroethylene over TiO2: products and mechanisms, Environ. Sci. Technol. 27 (1993) 732–740.

[45] J. Rashid, M.A. Barakat, S.L. Pettit, J.N. Kuhn, InVO4-TiO2 composites for visible light photocatalytic degradation of 2-chlorophenol in wastewater, Environ. Technol. 35 (2014) 2153–2159.